

# X-ray observations of PSR B1259–63 near the 2007 periastron passage

M. Chernyakova<sup>1\*</sup>, A. Neronov<sup>2,3</sup>, F. Aharonian<sup>1,4</sup>, Y. Uchiyama<sup>5</sup>, T. Takahashi<sup>6,7</sup>

<sup>1</sup>*DIAS, 31 Fitzwilliam Place, Dublin 2, Ireland*

<sup>2</sup>*ISDC, Chemin d'Ecogia 16, CH-1290 Versoix, Switzerland*

<sup>3</sup>*Geneva observatory, Ch. des Maillettes 51, 1290 Sauverny, Switzerland*

<sup>4</sup>*MPIKP, PO Box 103980, 69029 Heidelberg, Germany*

<sup>5</sup>*SLAC National Accelerator Laboratory, 2575 Sand Hill Road M/S 29, Menlo Park, CA 94025, USA.*

<sup>6</sup>*Institute of Space and Astronautical Science/JAXA, Sagamihara, Kanagawa 229-8510, Japan.*

<sup>7</sup>*Department of Physics, University of Tokyo, 7-3-1 Hongo, Bunkyo, Tokyo 113-0033, Japan.*

Received <date> ; in original form <date>

## ABSTRACT

PSR B1259–63 is a 48 ms radio pulsar in a highly eccentric 3.4 year orbit with a Be star SS 2883. Unpulsed  $\gamma$ -ray, X-ray and radio emission components are observed from the binary system. It is likely that the collision of the pulsar wind with the anisotropic wind of the Be star plays a crucial role in the generation of the observed non-thermal emission. The 2007 periastron passage was observed in unprecedented details with *Suzaku*, *Swift*, *XMM-Newton* and *Chandra* missions. We present here the results of this campaign and compare them with previous observations. With these data we are able, for the first time, to study the details of the spectral evolution of the source over a 2 months period of the passage of the pulsar close to the Be star. New data confirm the pre-periastron spectral hardening, with the photon index reaching a value smaller than 1.5, observed during a local flux minimum. If the observed X-ray emission is due to the inverse Compton (IC) losses of the 10 MeV electrons, then such a hard spectrum can be a result of Coulomb losses, or can be related to the existence of the low-energy cut-off in the electron spectrum. Alternatively, if the X-ray emission is a synchrotron emission of very high energy electrons, the observed hard spectrum can be explained if the high energy electrons are cooled by IC emission in Klein-Nishina regime. Unfortunately the lack of simultaneous data in the TeV energy band prevents us from making a definite conclusion on the nature of the observed spectral hardening and, therefore, on the origin of the X-ray emission.

**Key words:** pulsars : individual: PSR B1259–63 – X-rays: binaries – X-rays: individual: PSR B1259–63

## 1 INTRODUCTION

PSR B1259–63 is a  $\sim 48$  ms radio pulsar located in an eccentric ( $e \sim 0.87$ ), 3.4 year orbit with a Be star SS 2883 (Johnston et al. 1992). This system is known to be highly variable on an orbital time scale in radio (Johnston et al. (2005) and references therein), X-ray (Chernyakova et al. (2006) and references therein), and TeV (Aharonian et al. 2005) energy ranges. The orbital multi-wavelength variability pattern is determined by the details of the interaction of a relativistic pulsar wind with a strongly anisotropic wind of the companion Be star, composed of a fast, rarefied polar wind and a slow, dense equatorial decretion disk. The disk of the Be star in the PSR B1259–63 system is believed to be tilted with respect to the orbital plane. While the inclination of the disk is not

constrained, the line of intersection of the disk plane and the orbital plane is known to be oriented at about  $90^\circ$  with respect to the major axis of the binary orbit (Wex et al. 1998; Wang et al. 2004) and the pulsar passes through the disk twice per orbit.

The unpulsed radio emission from the system appears approximately at the moment of the pre-periastron entrance of the pulsar into the equatorial Be star disk. Within several days unpulsed radio emission sharply rises to a peak, and then slightly decreases, as the pulsar passes through periastron. The second peak is reached during the second, post-periastron disk crossing (Johnston et al. 1999, 2005; Connors et al. 2002).

ASCA observations of the PSR B1259–63 system in 1994 and 1995 have shown that, similar to the radio light curve, the X-ray light curve has two peaks around the periastron (Kaspi et al. 1995; Hirayama et al. 1999). The *XMM-Newton* observations of the source's orbital X-ray light curve, with a detailed monitoring of

\* E-mail: masha@cp.dias.ie

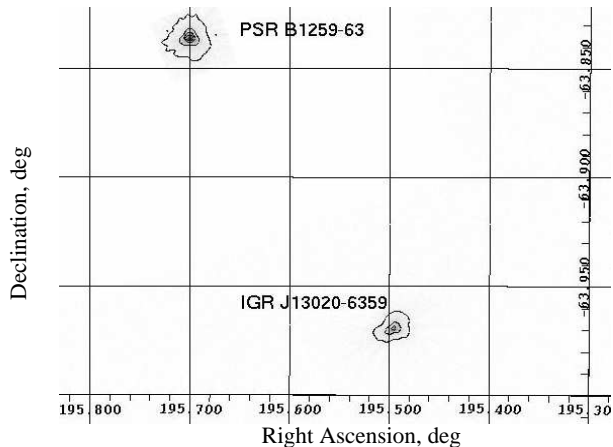


**Figure 1.** Contour plot of the MOS2 *XMM-Newton* field of view for the X12 observation in equatorial J2000 coordinates. A total of 4 contours were used with a square root scale between 5 counts per pixel (outer contour) and 500 counts per pixel (inner contour).

the period when pulsar approaches and enters the dense equatorial wind of the Be-star prior to periastron, have shown that the appearance of the unpulsed radio emission is also accompanied by a sharp rise of the X-ray flux (Chernyakova et al. 2006). The source spectral evolution has revealed an unexpected hardening of the source spectrum with the smallest value of the photon index  $\Gamma \sim 1.2$ , and a subsequent softening on the day scale as the pulsar moves deeper inside the disk. Unfortunately, in 2004 the source became invisible for *XMM-Newton* just after the entrance to the disk, so that the behaviour of the source within the disk and during the second disk crossing remained unclear. In order to clarify this behaviour, we organised an intensive X-ray monitoring campaign during the 2007 periastron passage. We have monitored the source with the *Suzaku*, *XMM-Newton*, *Chandra* and *Swift* satellites during a 2 months period, which covers both the pre- and post-periastron disk crossings. The results of this campaign are discussed below.

This paper is organized as follows: in Section 2 we describe the details of the data analysis. The results are presented in Section 3, and discussed in Section 4.

## 2 OBSERVATIONS AND DATA ANALYSIS

In 2007 we were able to organize an intensive X-ray monitoring campaign of the PSR B1259–63 system with *Suzaku*, *XMM-Newton*, *Chandra*, and *Swift*. The list of observations is given in Table 1, where  $\tau$  denotes the number of days after the periastron passage (27 July 2007, MJD 54308) and  $\phi$  is the true anomaly of the source.

### 2.1 *XMM-Newton* observations

In all *XMM-Newton* observations the source was observed with the European Photon Imaging Cameras (EPIC) MOS1, MOS2 (Den Herder et al. 2001) and PN (Struder et al. 2001) detectors in the small window mode with a medium filter. The *XMM-Newton* Observation Data Files (ODFs) were obtained from the online Science Archive<sup>1</sup> and analyzed with the Science Analysis Software

**Table 1.** Journal of 2007 of PSR B1259–63.

<i>XMM-Newton</i> observations							
Data Set	Date	MJD	$\tau$ (days)	$\phi$ (deg)	Exposure (ks)	f_mos1	f_mos2
X11	2007-07-08	54289	-19	86.14	9.34	$1.00^{+0.01}_{-0.01}$	$1.03^{+0.01}_{-0.01}$
X12	2007-07-16	54297	-11	112.26	36.54	$0.98^{+0.01}_{-0.01}$	$1.05^{+0.01}_{-0.01}$
X13	2007-08-17	54329	+21	278.57	6.35	$1.01^{+0.01}_{-0.01}$	$1.05^{+0.01}_{-0.01}$
<i>Chandra</i> observations							
Ch1	2007-07-28	54309	1	187.61	4.68		
Ch2	2007-08-06	54318	10	248.87	4.67		
Ch3	2007-08-24	54337	29	289.56	3.15		
Ch4	2007-09-18	54362	54	308.83	7.12		
<i>Swift</i> observations							
Sw1	2007-07-07	54288.6	-20	84.1	2.72		
Sw2	2007-07-09	54290.6	-18	88.3	5.13		
Sw3	2007-07-11	54292.3	-16	92.6	4.56		
Sw4	2007-07-13	54294.7	-14	99.5	4.34		
<i>Suzaku</i> observations							
Data Set	Date	MJD	$\tau$ (days)	$\phi$ (deg)	Exposure (ks)		
Sz1	2007-07-07	54288.6	-19.3	84.6	21.9		
Sz2	2007-07-09	54290.7	-17.2	88.1	19.5		
Sz3	2007-07-11	54292.6	-15.3	95.8	22.7		
Sz4	2007-07-13	54294.7	-13.2	102.2	22.9		
Sz5	2007-07-23	54304.3	-3.6	149.6	19.7		
Sz6	2007-08-03	54315.3	7.4	230.0	24.0		
Sz7	2007-08-18	54330.1	22.2	279.6	20.5		
Sz8	2007-09-05	54348.2	40.3	300.4	18.3		

(SAS) v7.1.2. During the data cleaning, all time intervals in which the count rate in the energy band above 10 keV was higher than 1 cts/sec for the PN detector and/or higher than 0.35 cts/sec for the MOS detectors, have been removed. In addition, we discarded the first kilosecond of X12 and the last two kiloseconds of X13 observations, as these were affected by soft proton flares.

The event lists for the spectral analysis were extracted from a 15'' radius circle at the source position for the X11 MOS1 observation, and from a 22.5'' radius circle for all other MOS and PN observations. We have performed spectral analysis by simultaneously fitting the data of MOS1, MOS2 and PN instruments, leaving the inter-calibration factors between the instruments free. The values of the MOS1 and MOS2 inter-calibration factors relative to the PN are given in last two columns of Table 1.

### 2.2 *Chandra* observations

During our 2007 monitoring campaign, PSR B1259–63 was observed with *Chandra* (Weisskopf et al. 2000) four times, see Table 1. The first two observations (Ch1 and Ch2) were done in the Faint mode with HETG grating. In order to reduce the pile-up, only 1/8 of the S3 detector was in use, which reduces the nominal frame integration time from 3.2 seconds to 0.4 seconds. The observations Ch3 and Ch4 were done in CC33\_FAINT mode, because of the higher expected source flux level. This allowed us to obtain good quality results not affected by a pile-up. Similar to the first two observations, only the S3 detector was in use. In the data analysis we used the *Chandra* Interactive Analysis of Observations software

<sup>1</sup> [http://xmm.vilspa.esa.es/external/xmm\\_data\\_acc/xsa/index.shtml](http://xmm.vilspa.esa.es/external/xmm_data_acc/xsa/index.shtml)

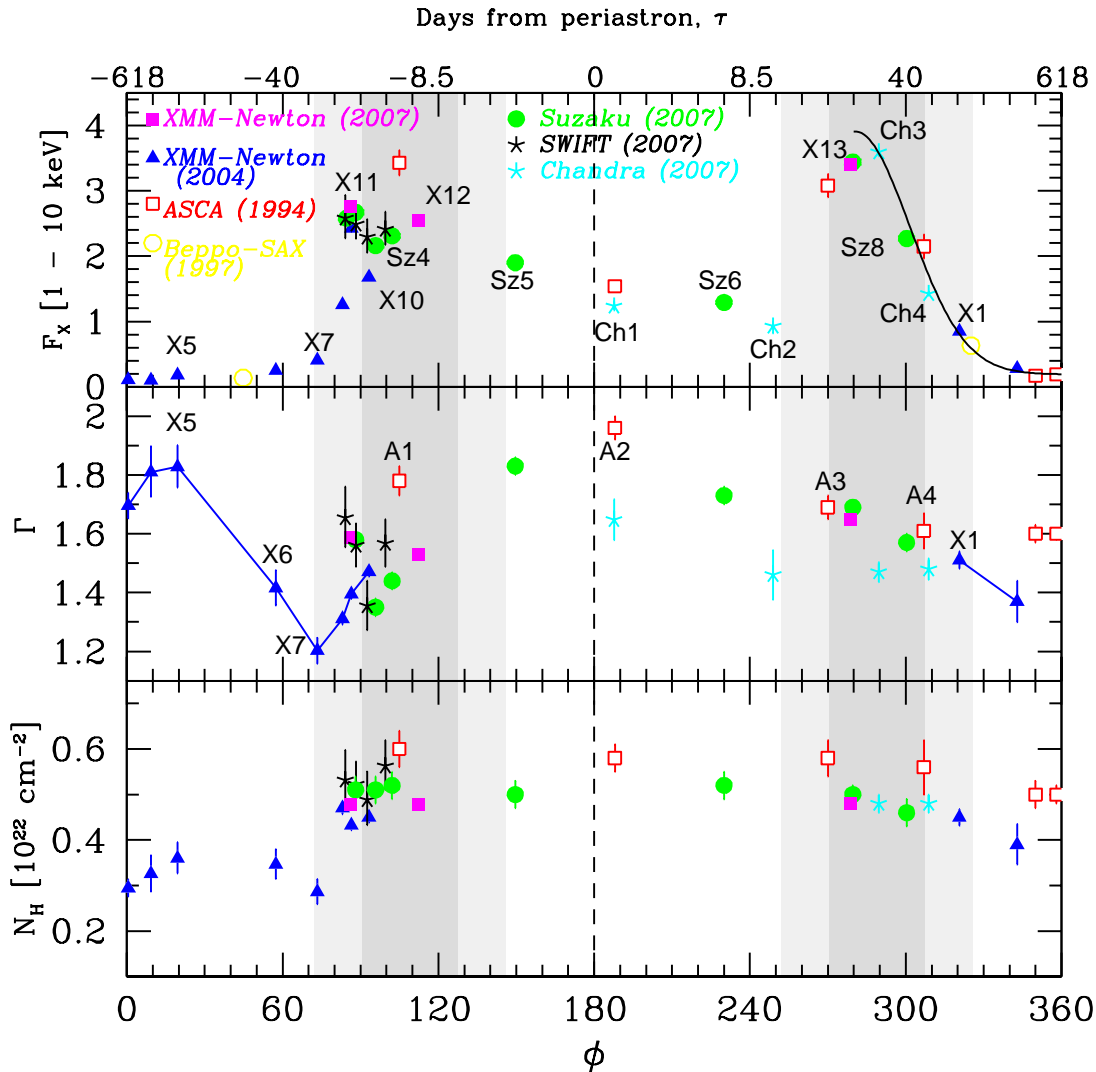


**Figure 2.** PSR B1259–63 orbital evolution of (1–10 keV) light curve (top panel), spectral index (middle panel) and hydrogen column density (bottom panel), as seen with *Suzaku*, *XMM-Newton*, *Swift* and *Chandra* during the 2007 periastron passage along with the old *XMM-Newton*, *BeppoSAX* and *ASCA* observations. 1 – 10 keV flux of the source is given in units of  $10^{-11}$  ergs  $\text{cm}^{-2}\text{s}^{-1}$ . Shaded area corresponds to the disk position proposed in Chernyakova et al. (2006). The solid line on the top panel is a fit with a Gaussian decay model (see text). To guide the eye we have connected old *XMM-Newton* data on the middle panel.

**Table 2.** Spectral parameters of IGR J13020–6359 during 2007 *Swift* and *XMM-Newton* observations.

Set	$F(2-10 \text{ keV})$ $10^{-11} \text{ ergs cm}^{-2}\text{s}^{-1}$	$\Gamma$	$N_H^*$ $10^{22} \text{ cm}^{-2}$	$\chi^2(\text{dof})$
Sw1	$2.10^{+0.65}_{-0.38}$	$1.00^{+1.18}_{-0.14}$	3.00	21.969 (11)
X11	$2.21^{+0.11}_{-0.19}$	$0.97^{+0.08}_{-0.06}$	$2.27^{+0.18}_{-0.12}$	171.08 (153)
Sw2	$2.33^{+0.87}_{-0.62}$	$1.21^{+0.20}_{-0.19}$	$2.56^{+0.46}_{-0.40}$	12.28 (22)
Sw3	$1.90^{+1.62}_{-0.64}$	$1.44^{+0.25}_{-0.57}$	$3.14^{+0.69}_{-0.57}$	7.28 (14)
Sw4	$1.83^{+1.33}_{-0.77}$	$1.67^{+0.35}_{-0.32}$	$3.96^{+1.15}_{-0.93}$	11.21 (11)
X12	$3.4^{+0.06}_{-0.09}$	$0.89^{+0.03}_{-0.02}$	$2.33^{+0.07}_{-0.05}$	534.78 (422)
X13	$2.89^{+0.10}_{-0.22}$	$0.87^{+0.07}_{-0.07}$	$2.32^{+0.13}_{-0.14}$	151.03 (150)

\* Due to the lack of statistics we fixed the value of  $N_H$  in the Sw1 observation.

package (CIAO ver. 3.4) and the CALDB version 3.4.0. The tool `celldetect` found no sources other than PSR B1259–63 in the field of view. We have used the generated region file for the spectral extraction, and collected background events from a nearby region of the same form and size. The resulting spectra were grouped to have at least 30 counts per energy bin. PSR B1259–63 showed a moderate level of activity, with an average count rate of 0.21 cts/s in Ch1 observations and 0.15 cts/s in Ch2 observation, which corresponds to a pile-up affection at the 15% and 10% levels, respectively<sup>2</sup> It is worth to noteworthy that Kishishita et al. (2009) in their analysis of Chandra LS 5039 data found that even a rel-

<sup>2</sup> Pile-up affection level was calculated using PIMMS v3.9d tool, available at <http://cxc.harvard.edu/toolkit/pimms.jsp>. Using this tool we assumed that emission can be described as an absorbed power law with parameters listed in Table 3.

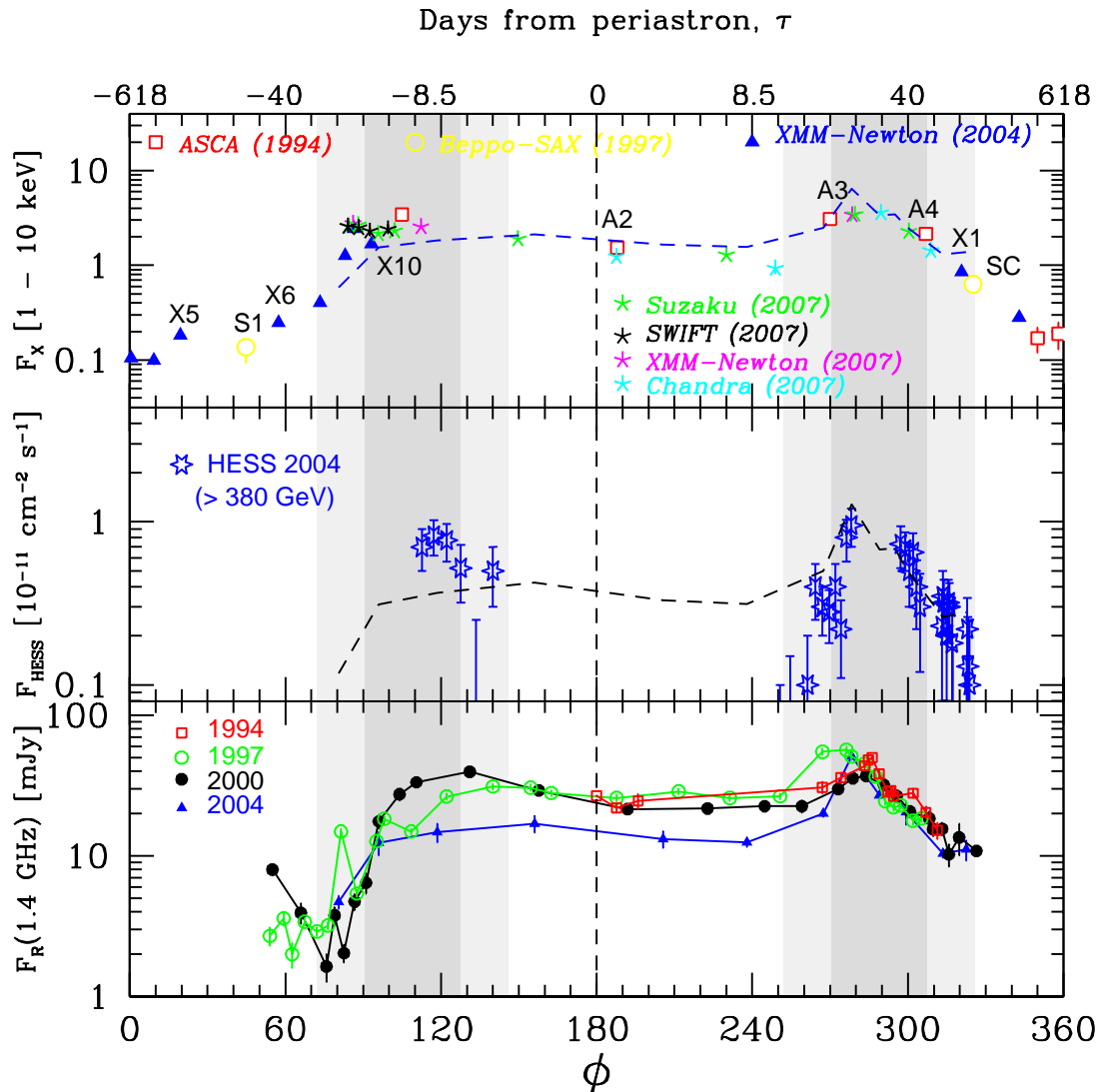


**Figure 3.** *Top panel:* PSR B1259–63 orbital light curve (1–10 keV), as seen with *Suzaku*, *XMM-Newton*, *Swift* and *Chandra* during the 2007 periastron passage along with the old *XMM-Newton*, *BeppoSAX* and *ASCA* observations. 1 – 10 keV flux of the source is given in units of  $10^{-11}$  ergs  $\text{cm}^{-2}\text{s}^{-1}$ . *middle panel:* 2004 HESS orbital light curve. *bottom panel:* Collection of historical 1.4 GHz radio light curve during different periastron passages. In order to compare the orbital behaviour at different wavelength we show with a black dash line the scaled 2004 radio curve on top and middle panels. Shaded area corresponds to the disk position proposed in Chernyakova et al. (2006).

ative small pile-up fraction can result in somewhat harder photon indexes. Thus the absolute numbers found for Ch1 and Ch2 should be treated with some care.

### 2.3 *Swift* observations

The *Swift*/XRT (Gehrels et al. 2004) data were taken in photon mode with a  $500 \times 500$  window size. We have processed all the data with standard procedures using the FTOOLS<sup>3</sup> task *xrtpipeline* (version 0.11.6 under the HEASoft package 6.4.0). We have extracted source events from a circular region with a radius of 20 pixels (1 pixel  $\approx 2.27''$ ). To account for the background, we have extracted events from a nearby circle of the same radius.

Due to the low count rate (less than 0.4 cts/s) no pile-up correction was needed. The spectral data were rebinned with a minimum of 25 counts per energy bin for the  $\chi^2$  fitting. The ancillary response file was generated with *xrtmkarf*, taking into account vignetting, and the point-spread function corrections. In our analysis we have used the *swxpc0to12s0\_20010101v010.rmf* spectral redistribution matrix for observations Sw1, Sw2 and Sw3 and the *swxpc0to12s6\_20010101v010.rmf* spectral redistribution matrix for the observation Sw4.

### 2.4 *Suzaku* observations

*Suzaku* has intensively monitored the PSR B1259–63 2007 periastron passage. Observations were performed with the X-ray Imaging spectrometer (XIS: Koyama et al. (2007)) and the Hard X-ray detector (HXD: Takahashi et al. (2007)). These data were first pre-

<sup>3</sup> See <http://heasarc.gsfc.nasa.gov/docs/software>

sented in Uchiyama et al. (2009). For completeness we present the list of *Suzaku* observations in Table 1.

### 3 RESULTS

#### 3.1 Imaging Analysis

X-ray emission from PSR B1259–63 has been clearly detected in all observations with all instruments. Apart from PSR B1259–63, another X-ray binary, IGR J13020-6359 (identified with 2RXP J130159.6-635806 in Chernyakova et al. (2005)), located 10 arcminutes away to the north-west, is detected in the MOS2 *XMM-Newton* and XRT *Swift* fields of view. Figure 1 shows the contour plot of *XMM-Newton* field of view for the X12 observation, in which both sources are visible. IGR J13020-6359 was not detected in MOS1, because some of its CCDs were turned off during the observation. This source is found to be in a low activity state, with the flux comparable to the flux of PSR B1259–63. Table 2 summarizes the spectral parameters of IGR J13020-6359 found in our observations.

#### 3.2 The X-ray light curve

The upper panel of Fig. 2 shows the X-ray orbital light curve of PSR B1259–63 system. The figure summarizes all the available X-ray data on the source in 1-10 keV energy range. The historical data of *XMM-Newton* (X1 – X10) and *BeppoSAX* points are taken from Chernyakova et al. (2006), *ASCA* data are taken from Hirayama et al. (1999). Observations made with different instruments at close orbital phases are consistent with each other, demonstrating satisfactory inter-calibration between different instruments: the points marking Sz1 and Sz2 and X11 and a *Swift* observation at the phase  $\theta \sim 85^\circ$  are superimposed on each other. Some of our new observations are done at orbital phases close to the ones of historical *ASCA* observations (e.g. Ch1). One can see that the system’s orbital light curve does not exhibit strong orbit-to-orbit variations - all fluxes measured by *ASCA* are consistent with the ones measured 13 years later. Our new data also confirm a local minimum at the phase  $\theta \approx 90^\circ$ , first observed with *XMM-Newton* during the 2004 periastron passage (X9 and X10 observations).

Stability of the orbital light curve allows us to use old and new data simultaneously while analyzing the flux orbital evolution. The first (pre-periastron) entrance of the pulsar into the equatorial disk of the Be star is accompanied by a sharp rise of the X-ray flux (points X7 - X9), by a factor of six in seven days ( $\Delta\theta = 13^\circ$ ). This period of the sharp rise of the flux is followed by a period of variability, most probably related to the interaction of the pulsar wind with the Be star disk. During this period, the X-ray flux decreases by a factor of 1.5 for two days ( $\Delta\theta = 7^\circ$ ) and then rises again for the subsequent two days ( $\Delta\theta = 6^\circ$ ). The decay of the flux after the exit of the pulsar from the disk is slower than the rise at the disk entrance. The flux decreases by a factor  $\sim 2.5$  up to the moment of the post-periastron entrance to the disk. The second entrance to the disk is again accompanied by a sharp rise of the flux, by a factor of 3.5 in less than ten days ( $\Delta\theta < 30^\circ$ ). The second peak is followed by an adiabatic decay with the characteristic decay scale of  $30^\circ$ , illustrated in Fig. 2 by solid curve, representing the best fit of the data with Gaussian decay model ( $f(\theta) = a * e^{-(\theta-\theta_0)^2/\Delta\theta_0^2} + c$ ,  $\theta_0 = 280^\circ, \Delta\theta_0 = 30^\circ$ ).

For comparison we also show in Fig. 3 the TeV light curve of 2004 HESS observation (Aharonian et al. 2005) and radio

**Table 3.** Spectral parameters for 2007 observations of PSR B1259–63.

Set	$\phi$	F*(1-10 keV)	$\Gamma$	$N_H^{**}$	$\chi^2$ (ndof)
Sw1	84.1	$2.58^{+0.36}_{-0.31}$	$1.65^{+0.1}_{-0.1}$	$0.53^{+0.07}_{-0.06}$	33 (35)
Sz1	84.58	$2.58 \pm 0.03$	$1.64 \pm 0.02$	$0.5 \pm 0.02$	375(354)
X11	86.14	$2.76^{+0.04}_{-0.04}$	$1.589^{+0.010}_{-0.010}$	$0.478^{+0.006}_{-0.006}$	1490 (1575)
Sw2	88.3	$2.49^{+0.25}_{-0.22}$	$1.56^{+0.07}_{-0.07}$	$0.52^{+0.05}_{-0.05}$	63 (654)
Sz2	88.10	$2.67 \pm 0.03$	$1.58 \pm 0.03$	$0.51 \pm 0.03$	321(309)
Sw3	92.6	$2.39^{+0.27}_{-0.24}$	$1.35^{+0.09}_{-0.08}$	$0.49^{+0.06}_{-0.06}$	41 (48)
Sz3	95.80	$2.16 \pm 0.03$	$1.35 \pm 0.03$	$0.51 \pm 0.03$	324(272)
Sw4	99.5	$2.41^{+0.27}_{-0.24}$	$1.57^{+0.08}_{-0.08}$	$0.56^{+0.06}_{-0.05}$	42 (53)
Sz4	102.17	$2.31 \pm 0.03$	$1.44 \pm 0.03$	$0.52 \pm 0.03$	387(298)
X12	112.26	$2.54^{+0.02}_{-0.02}$	$1.530^{+0.005}_{-0.005}$	$0.478^{+0.003}_{-0.003}$	2792 (2543)
Sz5	149.61	$1.90 \pm 0.02$	$1.83 \pm 0.03$	$0.50 \pm 0.03$	212(249)
Ch1	187.61	$1.24^{+0.06}_{-0.07}$	$1.65^{+0.07}_{-0.07}$	0.48	16(30)
Sz6	230.02	$1.29 \pm 0.02$	$1.73 \pm 0.03$	$0.52 \pm 0.03$	189(205)
Ch2	248.87	$0.93^{+0.06}_{-0.11}$	$1.46^{+0.08}_{-0.09}$	0.48	23 (22)
X13	278.57	$3.40^{+0.04}_{-0.04}$	$1.647^{+0.010}_{-0.009}$	$0.480^{+0.005}_{-0.005}$	1648 (1595)
Sz7	279.61	$3.44 \pm 0.04$	$1.69 \pm 0.02$	$0.50 \pm 0.02$	406(402)
Ch3	289.56	$3.59^{+0.06}_{-0.07}$	$1.47^{+0.03}_{-0.03}$	$0.48^{+0.02}_{-0.02}$	187 (196)
Sz8	300.35	$2.27 \pm 0.03$	$1.69 \pm 0.02$	$0.46 \pm 0.03$	283(253)
Ch4	308.83	$1.43^{+0.03}_{-0.03}$	$1.48^{+0.04}_{-0.04}$	$0.48^{+0.02}_{-0.02}$	193 (200)

\* In units of  $10^{-11}$  erg  $\text{cm}^{-2}$   $\text{s}^{-1}$ .

\*\* In units of  $10^{22}$   $\text{cm}^{-2}$ .

(Johnston et al. 1999; Connors et al. 2002; Johnston et al. 2005) light curves of different periastron passages. It is seen that the general flux behaviour (rapid rise at the disk entrance, followed by a slow decay) in all energy bands is similar. To make this point more clear we add the scaled radio light curve of 2004 periastron passage to panels showing the X-ray and TeV data (dashed line).

#### 3.3 Spectral Analysis

The spectral analysis was done with the NASA/GSFC XSPEC v11.3.2 software package. In Fig. 4 the folded and unfolded spectra of PSR B1259–63 for X12, Sw3, Ch2, and Ch3 observations are shown. In order to make the figure clear, we have multiplied the observed spectra by the specified factors.

A simple power law model with photoelectrical absorption describes the data well in most observations, with no evidence for any line features. In Table 3 we present the results of the three parameter fits to the *Suzaku*, *XMM-Newton*, *Chandra* and *Swift* data in the 0.5 – 10 keV energy range. The uncertainties are given at the  $1\sigma$  statistical level and do not include systematic uncertainties. The quality of the first two *Chandra* observations prevent the simultaneous determination of the spectral slope and absorption column density, so we decided to fix the latter to the value of  $N_H = 4.8 \times 10^{21} \text{cm}^{-2}$ , consistent with the value found in *XMM-Newton* observations. Orbital evolution of the spectral parameters is shown in Figure 2. The high value of the reduced  $\chi^2$  for Sz3 (1.19 for 272 d.o.f.) and Sz4 (1.30 for 298 d.o.f.) observations was studied in details in Uchiyama et al. (2009). It was found that for these observations broad band (0.6-50 keV) spectrum is much better fitted with a broken power law model with a spectral break from  $\Gamma_1 = 1.25 \pm 0.04$  below  $E_{br} \sim 5$  keV to  $\Gamma_2 = 1.6 \pm 0.05$  above.



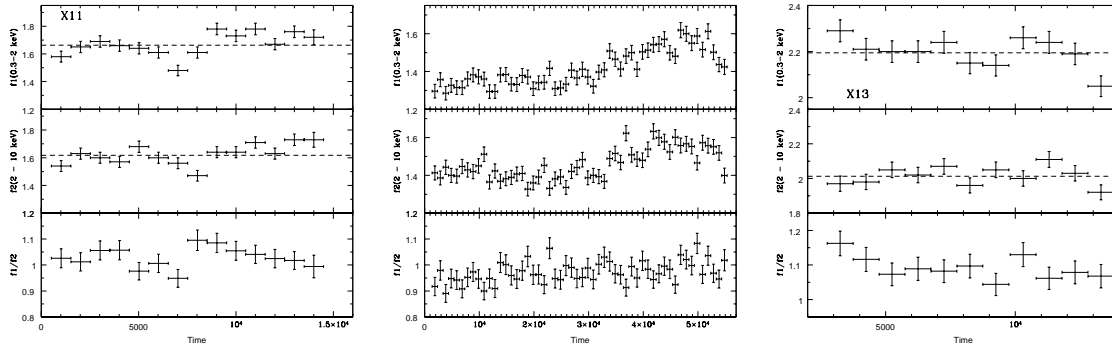


**Figure 5.** Light Curves of X11(left), X12(middle) and x13(right) observations in 0.3 - 2 keV (top panel), 2 - 10 keV (middle panel) along with hardness ratio (bottom panel). Time bin size is equal to 1ks. Dashed line indicates the best fit of the data with a constant model.

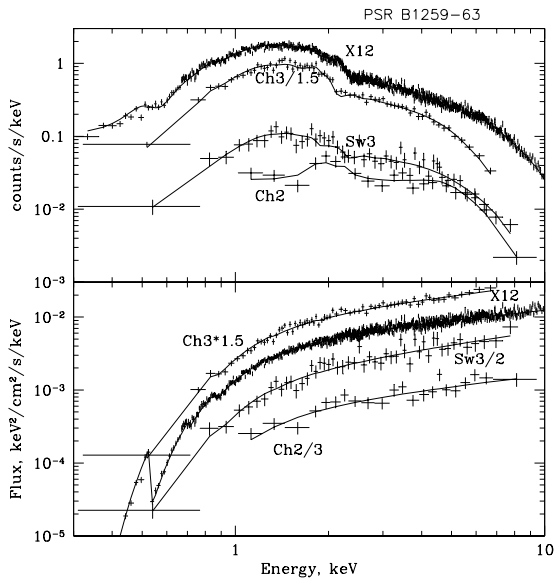


**Figure 4.** Folded(top panel) and unfolded (bottom panel) PSR B1259–63 spectra during the X12 (PN data), Sw3, Ch2 and Ch3 observations. In order to make the figure clearer we have multiplied the observed spectra by the specified factors.

### 3.4 Timing Analysis

Within one orbit PSR B1259–63 is known to be variable at different time scales. Apart from the orbital time scale (several years), fast, day-scale, variability of the flux and spectral characteristic is observed during the periastron passage. Variability at time scales much shorter than the orbital time scale is observed in other TeV binaries. For example, the X-ray emission from the binary LSI +61° 303 is characterized by a spectral energy distribution similar to the one of PSR B1259–63 (which might point to the similar mechanism of the X-ray emission) with variability time scales of down to  $\sim 1$  msec (Sidoli et al. 2006) and possibly even shorter (Smith et al. 2008). Such short time scale variability could be related to the clumpy structure of the wind of the Be star (Zdziarski et al. 2008). If so, then the clumpy structure of the Be star wind should also lead to the short-time scale variability of emission from the PSR B1259–63 system. In order to study

the variability on the short timescales, we have analyzed the light curves in the 0.3-2 keV and 2-10 keV energy ranges in individual X-ray observations.

Figure 5 shows the soft and hard energy band light curves (1ks time bins) of the three 2008 *XMM-Newton* observations of the source. The lower panels of this figure show the hardness ratios.

The source flux appears to be variable at the observation ( $\sim 10$  ksec) time scale at least in the X11 and X12 observations. In the case of the observation X11, the best fit of the soft (hard) band light curves with a constant flux, shown in the Figure 5, gives a  $\chi^2 = 55.88$  ( $\chi^2 = 42.52$ ) for 13 degrees of freedom. The probability that the soft (hard) band flux stayed constant over the entire observation is  $3 \times 10^{-7}$  ( $5 \times 10^{-5}$ ), i.e. the constant flux hypothesis is ruled out at a  $\sim 6\sigma$  ( $\sim 5\sigma$ ) level.

To study the details of variability at the  $\sim 10$  ks time scale, we arranged a long  $\sim 50$  ks continuous exposure during the observation X12. The flux of the source was stable (1.4 cts/s in 2-10 keV energy range) during the first  $\sim 30$  ks of the observation and then during the following 10 ks grew up to a count rate of 1.6 cts/s. No sharp variations of the flux and hardness ratio on the short time scales have been observed. No significant variations of the flux are detected in the *XMM-Newton* observation X13: the scatter of the data points in the light curve shown in the right panel of Fig. 5 does not exceed the  $3\sigma$  limit in the soft or the  $2\sigma$  limit in the hard energy bands.

A possible episode of faster ( $< 10$  ks time scale) flux variations was detected in the X11 observation, which is close to the moment of pulsar entrance into the disk and is in the middle of the period of strong spectral variability. In order to find the minimal variability time scale in this observation we have applied the structure function analysis (Simonetti et al. 1985) to the X-ray light curve.

Fig. 6 shows the structure functions calculated for the soft band light curve of X11 observation. The error bars of the structure function are estimated via the simulation of  $10^4$  light curves in which the values of the flux in each time bin are scattered around the measured values of the flux. The structure function deviates by  $3\sigma$  from the low plateau value at the time scale  $\tau \approx 3$  ks, which means that the light curve is variable at this time scale. For comparison we show, in the same figure, an example structure function of one of the simulated light curves, in which the flux variations are only due to the statistical uncertainty of the signal. One can see that the structure function of the simulated light curve is consistent with the lower plateau value in all the considered time range.

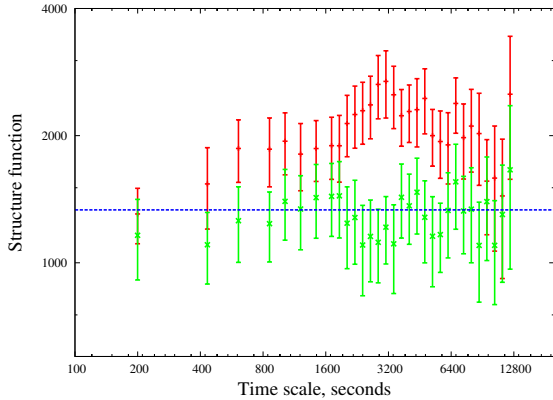


**Figure 6.** Red: structure function of the 0.3-2 keV band light curve of the observation X11. Dashed horizontal line shows the low plateau. Green: example of the structure function of a simulated light curve in which flux variations are due to the statistical scatter of the signal.

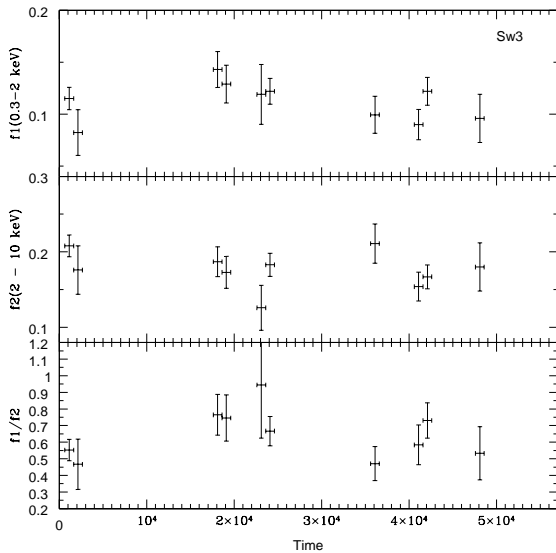


**Figure 7.** Light Curves of Sw3 observation in 0.3 - 2 keV (top panel), 2 - 10 keV (middle panel) along with hardness ratio (bottom panel). Time bin size is equal to 1ks.

Evidence of the variability of the source on the several kiloseconds time scale was also reported in some of ROSAT (Cominsky et al. 1994) and *Suzaku* (Uchiyama et al. 2009) observations.

An example of the *Swift* light curve during the Sw3 observation is shown in Figure 7. One can see that the source monitoring strategy was to take a set of  $\sim 1$  ks long snap-shots separated by longer (several kiloseconds) time intervals. From Fig. 7 one can see that no significant variability at the time scale  $\sim 10^4$  s is found in the *Swift* data.

#### 4 DISCUSSION

The 2007 observational campaign confirms the previous finding (Chernyakova et al. 2006) that during the first, pre-periastron pas-

sage of the disk, the X-ray spectrum of the source hardens on a day scale reaching a value of the photon index smaller than 1.5. During the 2004 periastron passage, a spectral state with photon index  $\Gamma_{\text{ph}} \simeq 1.2$  was observed at the beginning of the rapid growth of the X-ray flux at the disk entrance ( $\phi = 73^\circ$ ). Remarkable, the time of the subsequent spectral softening coincided with the time of a step-like increase of the hydrogen column density ( $\phi = 83^\circ$ ), which can be related to the penetration of the pulsar in the dense equatorial disk. The observed hardening, along with the successive softening and sharp flux rise, was attributed by Chernyakova et al. (2006) to the injection of high energy electrons at the disk entrance (e.g. due to the proton-proton collisions), or to a sharp decrease of the high energy electron’s escape velocity accompanied with the modification of their spectrum by Coulomb losses. An alternative explanation of the hard X-ray spectrum observed at the disk entrance is possible within a model in which X-ray emission is produced via the synchrotron mechanism (Khangulyan et al. 2007; Uchiyama et al. 2009). In this case hardening of the spectrum to photon indexes  $\Gamma_{\text{ph}} < 1.5$  on a day time scale can be achieved if the electron energy loss is dominated by inverse Compton (IC) scattering losses in the Klein-Nishina regime (Khangulyan & Aharonian 2005). The Klein-Nishina regime of IC scattering becomes important at energies above  $E_e \geq m_e^2 c^4 / (2.7kT_*) \sim 30$  GeV, where  $T_*$  is the temperature of the Be star. Decrease of the IC cross-section at high energies leads to the decrease of the efficiency of the IC cooling of electrons and, as a result, to the hardening of the electron spectrum. Electrons with a power law energy distribution  $N_e \propto E_e^{-\Gamma}$  cooled in the Klein-Nishina regime form a spectrum  $N_e(E_e) \propto E_e^{-\Gamma+1} \times \left[ \ln \frac{4EK T}{m_e^2 c^4} - \frac{2\Gamma}{\Gamma^2-1} - 0.6472 \right]^{-1}$ , much harder than  $N_e(E_e) \propto E_e^{-(\Gamma+1)}$  in Thompson limit (Blumenthal&Gould 1970). Thus the resulting synchrotron spectrum is proportional to  $e^{-\Gamma/2}$  and can be harder than 1.5.

The 2007 data did not cover the period of the entrance to the disk, so it is not possible to check if the spectral hardening preceding the flux growth repeats from orbit to orbit. Instead, the photon index  $\Gamma_{\text{ph}} \simeq 1.3$  was observed in 2007 at almost the maximum of the X-ray flare associated to the pre-periastron disk passage. More precisely, the time of the hardening and subsequent softening of the spectrum in the 2007 data coincides with a local “dip” in the X-ray light curve during the broad flare associated to the disk passage. No strong variations of the hydrogen column density are noticeable at the moment of the hardening of the spectrum. Detection of the spectral break in the X-ray spectrum of the source at  $E \simeq 5$  keV in *Suzaku* observation, which reveals the hard state with  $\Gamma_{\text{ph}} \simeq 1.3$  (Uchiyama et al. 2009), provides an additional clue for the understanding of the nature of the observed spectral hardening.

These two models of spectral hardening could be readily distinguished via multi-wavelength observations. In the case of the IC mechanism of the X-ray emission, the energies of electrons responsible for the X-ray emission are in the range of  $\sim 10$  MeV, while in the synchrotron model the X-ray emitting electrons have multi-TeV energies. A necessary condition for the hardening of the spectrum beyond  $\Gamma = 1.5$  in the synchrotron model is that the energy losses of multi-TeV electrons are dominated by the IC loss. This means that the expected TeV-band IC luminosity of the source at the moment of the spectral hardening is larger than the X-ray luminosity. Unfortunately, the absence of the TeV observations simultaneous with the X-ray observations in 2007 does not allow us to distinguish between the two models.

If the hard X-ray spectrum can be explained by Coulomb losses of the  $\sim 10$  MeV electrons, then the break at the

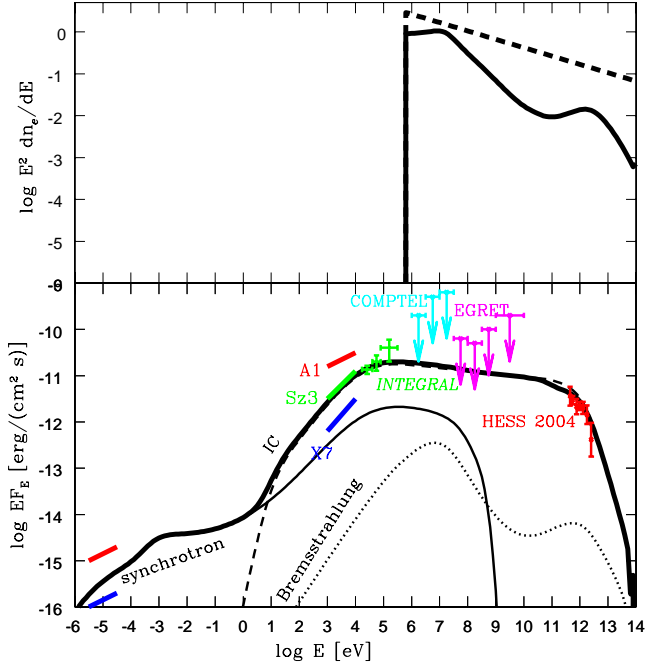


**Figure 8.** Spectral energy distribution of PSR B1259–63 in the model with the power law injection spectrum of electrons with spectral index  $\Gamma_e = 2.2$ . Top panel shows the initial electron injection spectrum with the dashed line and the spectrum formed in result of cooling and escape of electrons to the distance  $D \sim 10^{14}$  cm (solid line). Bottom panel shows the spectra of synchrotron (thin solid line), inverse Compton (dashed thin line) and bremsstrahlung emission (dotted thin line) as well as the overall spectrum modified by the pair production in the photon field of the Be star (thick solid line). Blue and red lines at the radio part of the spectrum illustrate the slope and possible flux range of the observed radio emission

$\sim 5$  keV energy, observed by Suzaku, has to be ascribed to the so-called “Coulomb” break in the electron spectrum. Such a break appears at the energy  $E_C$ , at which the rate of the Coulomb energy loss is equal to the IC energy loss rate:  $E_C \approx 15 \left[ D/10^{13} \text{ cm} \right] \left[ n_e/10^8 \text{ cm}^{-3} \right]^{1/2}$  MeV, where  $n_e$  is the stellar wind density at a distance  $D$  ( $10^{13}$  cm is a characteristic separation of the companions at orbital phases close to periastron). Electrons with the energy  $E_C$  produce IC emission in the energy band  $\epsilon_C \approx 4 \left[ T_*/3 \times 10^4 \text{ K} \right] \left[ E_C/10 \text{ MeV} \right]^2$  keV. Measurement of the break in the X-ray spectrum of the source enables an estimate of the density of the medium

$$n_e(D \approx 10^{13} \text{ cm}) \approx 10^8 \text{ cm}^{-3} \quad (1)$$

This estimate is consistent with the one expected for an equatorial disk with the radial density profile  $n_e(D) = n_0(D/R_*)^{-3.5}$  if the disk density close to the surface of the star is  $n_0 \sim 10^{12} \text{ cm}^{-3}$ .

If the X-ray emission is produced via the IC mechanism, the break in the X-ray spectrum can be also related to the existence of a low-energy cut-off in the electron spectrum. Indeed, the IC cooling time of the X-ray emitting electrons of the energy  $E$  is

$$\begin{aligned} t_{IC(T)} &= \frac{3\pi m_e^2 c^4 D^2}{\sigma_T L_* E} \\ &\approx 6 \times 10^5 \left[ \frac{10^{38} \text{ erg s}^{-1}}{L_*} \right] \left[ \frac{D}{10^{13} \text{ cm}} \right]^2 \left[ \frac{10 \text{ MeV}}{E_e} \right] \text{ s} \end{aligned} \quad (2)$$

where  $L_*$  is the luminosity of the Be star,  $m_e$  is the electron mass and  $\sigma_T$  is the Thomson cross-section. The IC cool-

ing time is comparable to the escape time  $t_{\text{esc}} \approx D/V \approx 10^6 \left[ D/10^{13} \text{ cm} \right] \left[ V/10^7 \text{ cm/s} \right] \text{ s}$  if the escape velocity is  $V \sim 10^7$  cm/s. If the IC emitting electrons are initially injected at energies much larger than 10 MeV (e.g. as a result of the proton-proton interactions, Neronov & Chernyakova (2007)), they would not be able to cool to energies below  $\sim 10$  MeV, which can explain the deficiency of the IC emission at the energies below the  $\sim 5$  keV break energy.

Finally, the shape of electron spectrum below 10 MeV can be also affected by adiabatic cooling. Equating the adiabatic cooling rate  $dE_e/dt = (E_e/R)dR/dt = nV E_e/(2D)$ , where  $R \sim D^{n/2}$  is the radius of the synchrotron/IC emitting bubble and  $V$  is the escape velocity, to the IC cooling rate,  $dE_e/dt = (4/3)\sigma_T c U_{\text{ph}}(E_e/m_e c^2)^2$ , where  $U_{\text{ph}} = L_*/4\pi D^2 c$  is the radiation energy density, one finds the adiabatic break energy

$$E_{\text{ad}} \approx 10 \text{ MeV} \left[ \frac{D}{10^{13} \text{ cm}} \right] \left[ \frac{V}{10^7 \text{ cm/s}} \right] \left[ \frac{L_*}{10^{38} \text{ erg/s}} \right]^{-1} \text{ eV} \quad (3)$$

If the emission is produced at the distances  $D \sim 10^{13}$  cm, the observation of the cooling break at the energy  $\epsilon \approx 5$  keV is consistent with the assumption that the break is produced by the influence of the adiabatic losses if the escape velocity is  $V \sim 10^7$  cm/s, which is in agreement with the estimates of the velocity of the stellar wind in the considered range of distances (Waters, Coté & Lamers 1987).

The results of numerical modeling of the broad band spectrum of the source within the IC scenario of the X-ray emission are shown in Fig. 8. We assume that the high energy electrons are injected in the synchrotron/IC emitting bubble, which escapes with a speed equal to the speed of the stellar wind. The spectrum of the high-energy electrons, shown by the thick solid line in the upper panel of Fig. 8, is formed as a result of cooling of electrons due to the IC, synchrotron, bremsstrahlung and Coulomb energy losses during their escape from the system. The injection of electrons is assumed to happen at a distance  $D_0 = 3 \times 10^{12}$  cm. The injection spectrum of the electrons, shown by the dashed line in the upper panel of the figure is assumed to be a power law with spectral index  $\Gamma_{\text{inj}} = 2.2$  (Kirk et al. 2000). The magnetic field is assumed to be equal to  $B_0 = 0.1$  G at the initial injection distance. In the calculations presented in Fig. 8 we have used the angle-averaged IC cross-section to calculate the IC energy loss and emission spectrum. The account of the anisotropy of the IC emission is important for the accurate calculations of the source light curve (see Chernyakova & Illarionov (1999); Khangulyan et al. (2008)), but requires a detailed 3D model and is not addressed here for simplicity. The cooled spectrum of electrons is shown on the top panel of Fig. 8 with a solid line. Coulomb losses affect the electron spectrum at the lower end, leading to the formation of the first bump. The second bump arises due to the decrease of the cross-section after the transition from Thomson to the Klein-Nishina regime, which results in spectral hardening above  $10^{11}$  eV, and softening above  $10^{12}$  eV because of the dominance of the synchrotron losses at those energies.

An alternative model, in which the observed X-rays are produced via the synchrotron mechanism is illustrated in Fig. 9. For the calculation we have used the same numerical code as for the calculation shown in Fig. 8. The main differences between the two cases are different injection spectra and the assumed initial values of the magnetic field. The magnetic field at the initial distance  $D = 3 \times 10^{12}$  cm is assumed to be  $B_0 = 1$  G. The electron injection spectrum, shown by the dashed line in the upper panel of Fig. 9 is assumed to be sharply peaked at energies about  $10^{13}$  eV. If the typical initial electron injection energies are above 10 TeV, the shape of



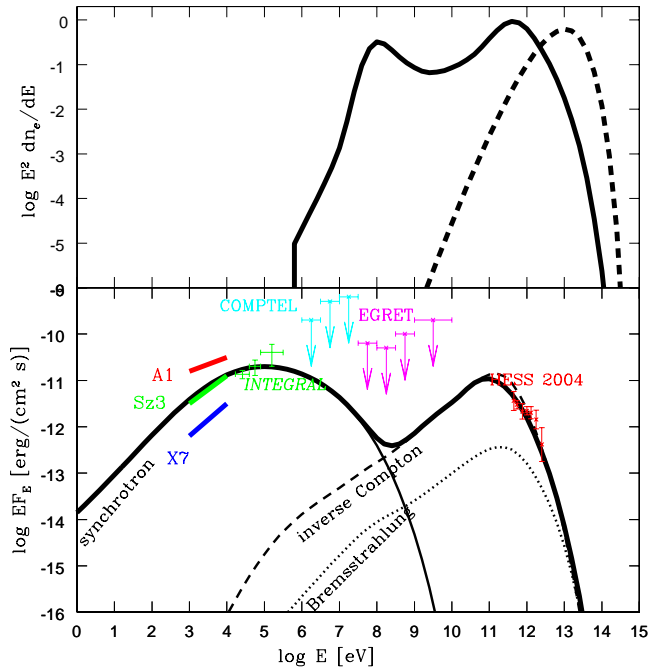


**Figure 9.** Spectral energy distribution of PSR B1259–63 in the model with electron injection at very high energies. Notations are the same as in Fig. 8.

the cooled electron spectrum at the energies below 10 TeV is completely determined by the cooling effects and is almost independent of the details of the initial electron injection spectrum.

The low-energy cut-off in the cooled electron spectrum at  $E \sim 10^8$  eV arises because at energies below  $10^8$  eV the radiative cooling time of electrons becomes longer than the escape time from the system. The spectrum of electrons is hard in the 10 GeV - 1 TeV energy interval, in which the electron energy losses are dominated by IC scattering proceeding in the Klein-Nishina regime. A sharp break in the spectrum at TeV energies is related to the fact that the cooling rate of the multi-TeV electrons is determined by the synchrotron, rather than IC energy losses. The break energy can be determined by equating the synchrotron loss time

$$t_S = \frac{6\pi m_e^2 c^3}{\sigma_T B^2 E_e} \approx 4 \times 10^2 \left[ \frac{1G}{B} \right]^2 \left[ \frac{1 \text{ TeV}}{E_e} \right] \text{ s} \quad (4)$$

to the IC loss time in the Klein-Nishina regime,

$$\begin{aligned} t_{KN} &\approx \frac{16E_e D^2 \hbar}{\sigma_T (m_e c k T_\star R_\star)^2} \ln^{-1} \frac{0.55 E_e k T_\star}{m_e^2 c^4} \\ &\approx 10^3 \left[ \frac{E_e}{1 \text{ TeV}} \right] \left[ \frac{D}{10^{13} \text{ cm}} \right] \text{ s} \end{aligned} \quad (5)$$

This gives

$$E_{br} = 0.5 \left[ \frac{B}{1 \text{ G}} \right] \left[ \frac{D}{10^{13} \text{ cm}} \right]^{-1/2} \text{ TeV} \quad (6)$$

The synchrotron emission produced by electrons with the energy  $E_{br}$  is emitted at the energy

$$\epsilon_S = \frac{e \hbar B E_e^2}{m_e^2 c^5} \approx 10 \left[ \frac{B}{1 \text{ G}} \right] \left[ \frac{E_e}{0.5 \text{ TeV}} \right]^2 \text{ keV} \quad (7)$$

which is close to the observed break energy  $\epsilon \approx 5$  keV in the *Suzaku* spectrum.

The two different mechanisms of the X-ray emission (IC or synchrotron) could also be distinguished by the difference in the

variability properties of the X-ray signal expected in the two models. In principle, much faster variability is expected in the synchrotron model of X-ray emission. Within this model, the typical variability time scale is set up by the synchrotron and IC cooling times of the multi-TeV electrons. This time scale could be as short as  $\leq 1$  ks, if the magnetic field in the emission region is strong enough. On the other hand, within the IC model of X-ray emission, the characteristic variability time scales are set up by the rate of the Coulomb and/or IC and/or adiabatic energy losses of  $\sim 10$  MeV electrons, which are normally much longer than  $\sim 1$  ks. The detection of the variability in the X11 observation of *XMM-Newton* at the time scale of  $\sim 3$  ks thus provides an argument in favor of the synchrotron model of the X-ray emission. However, fast variability in the X11 observation is detected at a  $3\sigma$  level with the help of the structure function analysis. Further observations are necessary to firmly establish the presence/absence of the fast variability of the X-ray emission.

To summarize, we find that the X-ray data alone do not allow us to distinguish between the synchrotron and IC origin of the X-ray emission from the source. The observation of the hardening of the spectrum below  $\Gamma = 1.5$  during the pre-periastron disk passage gives an important clue about the X-ray emission mechanism. However, the origin of the observed spectral hardening can be clarified with the help of the simultaneous TeV observations. If the observed X rays have an IC origin, then the observed hardening during the drop of the flux is primarily connected to the hardening of electron spectrum below  $\sim 10$  MeV (due to the Coulomb losses, or because of the escape of electrons from the emission region), so that no tight correlation between the X-ray spectral evolution and the TeV energy band emission is expected. On the other hand, in the case of synchrotron origin of the observed X-rays, the spectral hardening can be produced if the electron cooling is dominated by the IC energy loss in the Klein-Nishina regime. This implies that the IC flux from the system in the very-high-energy band at the moment of the spectral hardening should dominate over the X-ray flux. GeV data can give us another possibility to distinguish between the models, as in this region the predicted flux value is very different in IC and synchrotron model. Hopefully *Fermi* Gamma-ray telescope observations of the next PSR B1259–63 periastron passage will give us a clue to the distinguish between the models.

## 5 ACKNOWLEDGMENTS

Authors are grateful to the unknown referee for valuable comments.

## REFERENCES

- Aharonian F. et al., *A&A*, 442, 1
- Blumenthal G.R.&Gould R.J., 1970, *Rev. Mod. Phys.*, 42, 237
- Cominsky L., Roberts M., Johnston S., 1994, *ApJ*, 427, 978
- Connors T.W., Johnston S., Manchester R. N., McConnell D., 2002, *MNRAS*, 336, 1201
- Chernyakova M. A., Illarionov A. F., 1999, *MNRAS*, 304, 359
- Chernyakova M., Lutovinov A., Rodriguez J., Revnivtsev M., 2005, *MNRAS*, 364, 455
- Chernyakova M., Neronov A., Lutovinov A., Rodriguez J., Revnivtsev M., 2006, *MNRAS*, 367, 1201
- den Herder J. W., Brinkman A. C., Kahn S. M., et al. 2001, *A&A*, 365, L7
- Gehrels N., et al., 2004, *ApJ* 611, 1005.

- Gould R.J., 1975, *ApJ.*, 196, 689
- Johnston S., Manchester R.N., Lyne A., Bailes M., Kaspi V. M., Qiao Guojun, D'Amico N., 1992, *ApJ*, 387, L37
- Johnston S. Manchester R.N., McConnell D., Campbell-Wilson D., 1999, *MNRAS*, 302, 277
- Johnston S., Ball L., Wang N., Manchester R. N., 2005, *MNRAS*, 358, 1069
- Hirayama M., Cominsky L. R., Kaspi V. M., Nagase F., Tavani M., Kawai N., Grove J. E., 1999, *ApJ*, 521, 718
- Kaspi V. M., Tavani M., Nagase F., Hirayama M., Hoshino M., Aoki T., Kawai N., Arons J., 1995, *ApJ*, 453, 424
- Khangulyan D., Aharonian F., 2005, *AIPC*, 745, 359
- Khangulyan D.; Hnatic S.; Aharonian F.; Bogovalov S., 2007, *MNRAS*, 380, 320.
- Khangulyan D., Aharonian F., Bosch-Ramon V., 2008, *MNRAS*, 383, 467
- Kirk J. G. , Guthman W., Gallant Y.A., Achterberg A., 2000, *ApJ* 542, 235
- Kishishita T., Tanaka T., Uchiyama Y., Takahashi T., 2009, *ApJ*, 697, 1
- Koyama K., et al., 2007, *PASJ*, 59, S23
- Neronov A., Chernyakova M., 2007, *Ap&SS*, 309, 253
- Paredes J.M., Mari J., Estalella R., Sarrate J., 1991, *A&A*, 248, 124,
- Sidoli L., Pellizzoni A., Vercellone S., Moroni M., Mereghetti S., Tavani M., 2006, *A&A*, 459, 901
- Smith A., et al., 2008, *arXiv:0809.4254*.
- Strüder L., Briel U., Dennerl K., et al., 2001, *A&A*, 365, L18.
- Simonetti J.H., Cordes J.M., Heeschen D.S., 1985, *ApJ.*, 296, 46.
- Takahashi T., et al., *PASJ*, 2007, 59, S35
- Tavani M., Arons J., *ApJ*, 1997, 477, 439
- Uchiyama Y., Tanaka T., Takahashi T., Mori K., Nakazawa K., 2009, accepted to *ApJ* (2009arXiv0904.1238)
- Wang N., Johnston S., Manchester R.N., 2004 *MNRAS*, 351, 599
- Wex N., Johnston S., Manchester R. N., Lyne A. G., Stappers B. W., Bailes M., 1998, *MNRAS* 298, 997
- Waters L.B.F.M., Coté J., Lamers H.J.G.L.M., 1987, *A&A*, 185, 206.
- Weisskopf M.C., Tananbaum H.D., Van Speybroeck L.P., O'Dell S.L., 2000, *SPIE* 4012, 1 (astro-ph/0004127)
- Zdziarski A., Neronov A., Chernyakova M., submitted to *MNRAS*, 2008arXiv0802.1174